



Publication Year	2020
Acceptance in OA	2021-11-16T15:41:42Z
Title	Properties of the dense core population in Orion B as seen by the Herschel Gould Belt survey
Authors	Könyves, V., André, Ph., Arzoumanian, D., Schneider, N., Men'shchikov, A., Bontemps, S., Ladjelate, B., Didelon, P., PEZZUTO, Stefano, BENEDETTINI, Milena, Bracco, A., Di Francesco, J., Goodwin, S., Rygl, K. L. J., Shimajiri, Y., SPINOGLIO, Luigi Giuseppe Maria, Ward-Thompson, D., White, G. J.
Publisher's version (DOI)	10.1051/0004-6361/201834753
Handle	http://hdl.handle.net/20.500.12386/31091
Journal	ASTRONOMY & ASTROPHYSICS
Volume	635

Properties of the dense core population in Orion B as seen by the *Herschel* Gould Belt survey^{★,★★}

V. Könyves^{1,2}, Ph. André¹, D. Arzoumanian^{3,4}, N. Schneider⁵, A. Men'shchikov¹, S. Bontemps⁶, B. Ladjelate⁷, P. Didelon¹, S. Pezzuto⁸, M. Benedettini⁸, A. Bracco⁹, J. Di Francesco^{10,11}, S. Goodwin¹², K. L. J. Rygl¹³, Y. Shimajiri¹, L. Spinoglio⁸, D. Ward-Thompson², and G. J. White^{14,15}

¹ Laboratoire d'Astrophysique (AIM), CEA/DRF, CNRS, Université Paris-Saclay, Université Paris Diderot, Sorbonne Paris Cité, 91191 Gif-sur-Yvette, France

e-mail: pandre@cea.fr

² Jeremiah Horrocks Institute, University of Central Lancashire, Preston PR1 2HE, UK

e-mail: vkonyves@uclan.ac.uk

³ Department of Physics, Graduate School of Science, Nagoya University, Nagoya 464-8602, Japan

⁴ Instituto de Astrofísica e Ciências do Espaço, Universidade do Porto, CAUP, Rua das Estrelas, PT4150-762 Porto, Portugal

⁵ I. Physik. Institut, University of Cologne, Cologne, Germany

⁶ Laboratoire d'Astrophysique de Bordeaux – UMR 5804, CNRS – Université Bordeaux 1, BP 89, 33270 Floirac, France

⁷ Instituto de Radioastronomía Milimétrica (IRAM), Av. Divina Pastora 7, Núcleo Central, 18012 Granada, Spain

⁸ Istituto di Astrofisica e Planetologia Spaziali-INAF, Via Fosso del Cavaliere 100, 00133 Roma, Italy

⁹ Laboratoire de Physique de l'École Normale Supérieure, ENS, Université PSL, CNRS, Sorbonne Université, Université de Paris, Paris, France

¹⁰ Department of Physics and Astronomy, University of Victoria, PO Box 355, STN CSC, Victoria, BC, V8W 3P6, Canada

¹¹ National Research Council Canada, 5071 West Saanich Road, Victoria, BC, V9E 2E7, Canada

¹² Department of Physics and Astronomy, University of Sheffield, Hounsfield Road, Sheffield S3 7RH, UK

¹³ INAF–Istituto di Radioastronomia, and Italian ALMA Regional Centre, Via Gobetti 101, 40129 Bologna, Italy

¹⁴ Department of Physics and Astronomy, The Open University, Walton Hall, Milton Keynes, MK7 6AA, UK

¹⁵ RAL Space, STFC Rutherford Appleton Laboratory, Chilton, Didcot, Oxfordshire, OX11 0QX, UK

Received 30 November 2018 / Accepted 29 September 2019

ABSTRACT

We present a detailed study of the Orion B molecular cloud complex ($d \sim 400$ pc), which was imaged with the PACS and SPIRE photometric cameras at wavelengths from 70 to 500 μm as part of the *Herschel* Gould Belt survey (HGBS). We release new high-resolution maps of column density and dust temperature for the whole complex, derived in the same consistent manner as for other HGBS regions. In the filamentary subregions NGC 2023 and 2024, NGC 2068 and 2071, and L1622, a total of 1768 starless dense cores were identified based on *Herschel* data, 490–804 (~ 28 –45%) of which are self-gravitating prestellar cores that will likely form stars in the future. A total of 76 protostellar dense cores were also found. The typical lifetime of the prestellar cores was estimated to be $t_{\text{pre}}^{\text{OrionB}} = 1.7^{+0.8}_{-0.6}$ Myr. The prestellar core mass function (CMF) derived for the whole sample of prestellar cores peaks at $\sim 0.5 M_{\odot}$ (in $dN/d\log M$ format) and is consistent with a power-law with logarithmic slope -1.27 ± 0.24 at the high-mass end, compared to the Salpeter slope of -1.35 . In the Orion B region, we confirm the existence of a transition in prestellar core formation efficiency (CFE) around a fiducial value $A_{\text{V}}^{\text{bg}} \sim 7$ mag in background visual extinction, which is similar to the trend observed with *Herschel* in other regions, such as the Aquila cloud. This is not a sharp threshold, however, but a smooth transition between a regime with very low prestellar CFE at $A_{\text{V}}^{\text{bg}} < 5$ and a regime with higher, roughly constant CFE at $A_{\text{V}}^{\text{bg}} \gtrsim 10$. The total mass in the form of prestellar cores represents only a modest fraction ($\sim 20\%$) of the dense molecular cloud gas above $A_{\text{V}}^{\text{bg}} \gtrsim 7$ mag. About 60–80% of the prestellar cores are closely associated with filaments, and this fraction increases up to $>90\%$ when a more complete sample of filamentary structures is considered. Interestingly, the median separation observed between nearest core neighbors corresponds to the typical inner filament width of ~ 0.1 pc, which is commonly observed in nearby molecular clouds, including Orion B. Analysis of the CMF observed as a function of background cloud column density shows that the most massive prestellar cores are spatially segregated in the highest column density areas, and suggests that both higher- and lower-mass prestellar cores may form in denser filaments.

Key words. stars: formation – ISM: clouds – ISM: structure – ISM: individual objects: Orion B complex – submillimeter: ISM

1. Introduction

Following initial results from the *Herschel* Gould Belt survey (HGBS; see André et al. 2010), the first complete study of

* Full Tables A.1 and A.2 are only available at the CDS via anonymous ftp to cdsarc.u-strasbg.fr (130.79.128.5) or via <http://cdsarc.u-strasbg.fr/viz-bin/cat/J/A+A/635/A34>

** *Herschel* is an ESA space observatory with science instruments provided by European-led Principal Investigator consortia and with important participation from NASA.

dense cores based on *Herschel* data in the Aquila cloud complex confirmed, with high number statistics, that the prestellar core mass function (CMF) is very similar in shape to the initial mass function (IMF) of stellar systems and that there is approximately one-to-one mapping between these two mass distributions (Könyves et al. 2015). Similar trends between the prestellar CMF and the stellar IMF can also be seen in the Taurus L1495 (Marsh et al. 2016), Corona Australis (Bresnahan et al. 2018), Lupus (Benedettini et al. 2018), and Ophiuchus (Ladjelate et al. 2019) clouds. These “first-generation” papers

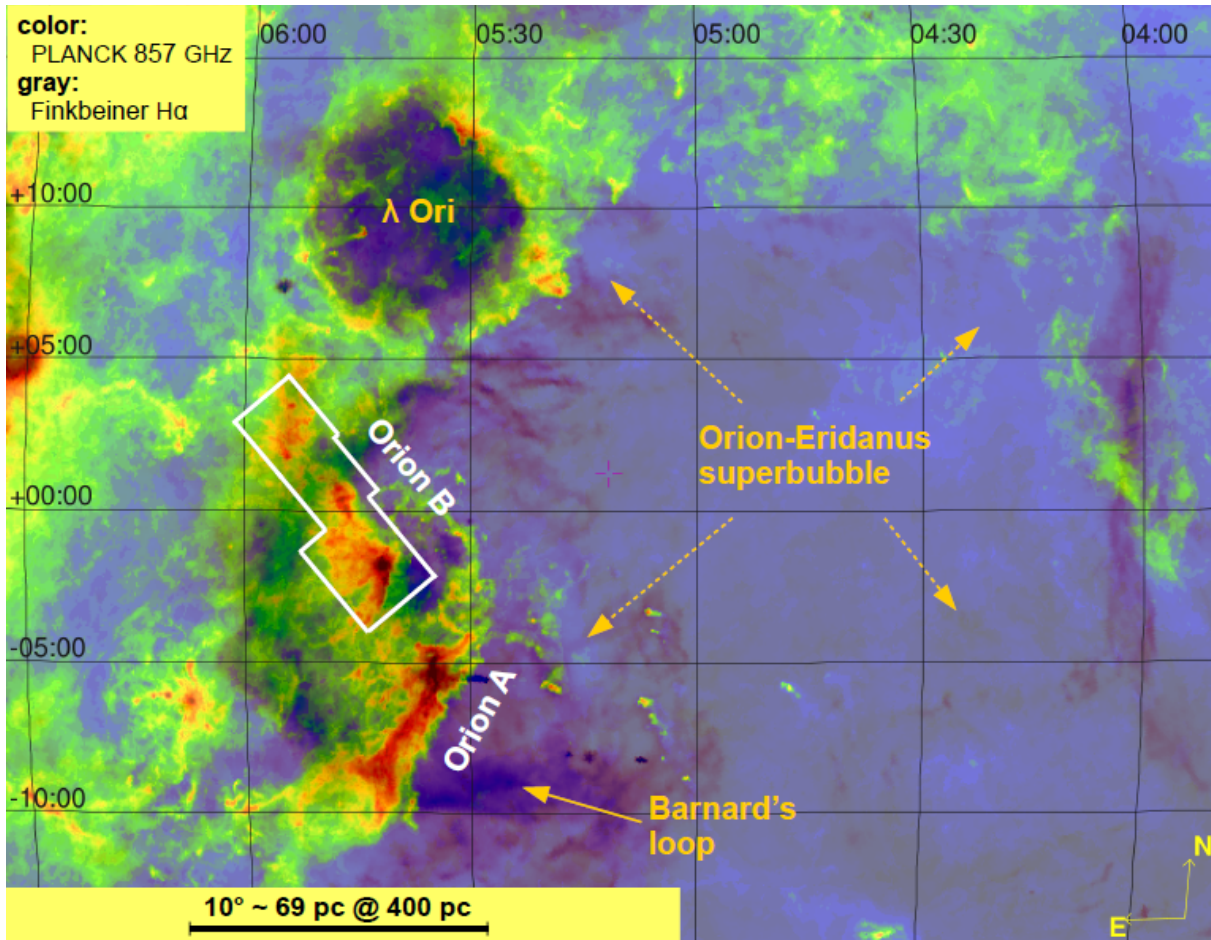


Fig. 1. Large-scale view of the Orion-Eridanus superbubble (which reaches beyond Barnard’s Loop) and star-forming clouds along its wall. The color background shows *Planck* 857 GHz (350 μm) emission (Public Data Release 2, PR2), and the overplotted gray features represent $\text{H}\alpha$ emission (Finkbeiner 2003). The region analyzed in this paper is outlined in white. (PR2 is described in the *Planck* 2015 Release Explanatory Supplement which is available at <https://wiki.cosmos.esa.int/planckpla2015/>).

from the HGBS include complete catalogs of dense cores and also demonstrate that the spatial distribution of dense cores is strongly correlated with the underlying, ubiquitous filamentary structure of molecular clouds. Molecular filaments appear to present a high degree of universality (Arzoumanian et al. 2011, 2019; Koch & Rosolowsky 2015) and play a key role in the star formation process. Additional specific properties of filaments based on *Herschel* imaging data for closeby ($d < 3$ kpc) molecular clouds are presented in Hennemann et al. (2012) on the DR21 ridge in Cygnus X, in Benedettini et al. (2015) on Lupus, and in Cox et al. (2016) on the Musca filament.

Overall, the combined properties of filamentary structures and dense cores observed with *Herschel* in nearby clouds support a scenario in which the formation of solar-type stars occurs in two main steps (André et al. 2014). First, the dissipation of kinetic energy in large-scale magneto-hydrodynamic (MHD) compressive flows generates a quasi-universal web of filamentary structures in the cold interstellar medium (ISM); second, the densest molecular filaments fragment into prestellar cores by gravitational instability, and then evolve into protostars. Furthermore, our *Herschel* findings on the prestellar core formation efficiency (CFE) in the Aquila molecular cloud (Könyves et al. 2015), coupled with the relatively small variations in the star formation efficiency (SFE) per unit mass of dense gas observed

between nearby clouds and external galaxies (e.g., Lada et al. 2012; Shimajiri et al. 2017), suggest that the filamentary picture of star formation proposed for nearby galactic clouds may well apply to extragalactic giant molecular clouds (GMCs) as well (André et al. 2014; Shimajiri et al. 2017).

Here, we present a detailed study of the dense core population in the Orion B molecular cloud based on HGBS data. With little doubt, Orion is the best studied star-forming region in the sky, and also the nearest site with ongoing low- and high-mass star formation (for an overview see Bally 2008). The complex is favorably located for us in the outer boundary of the Gould Belt where confusion from foreground and background gas is minimized; it lies toward the outer Galaxy and below the galactic plane at an average distance of about 400 pc from the Sun (Menten et al. 2007; Lallement et al. 2014; Zucker et al. 2019), which is the distance adopted in this paper.

Most of the famous clouds in the Orion region (Fig. 1) seem to scatter along the wall of the so-called Orion-Eridanus superbubble (“Orion’s Cloak”, see e.g., Bally 2008; Ochsendorf et al. 2015; Pon et al. 2016), which was created by some of Orion’s most massive members that died in supernova explosions. This enormous superbubble spans ~ 300 pc in diameter (Bally 2008) with some nested shells inside, among which, for example, the Barnard’s Loop bubble and the λ Ori bubble (see

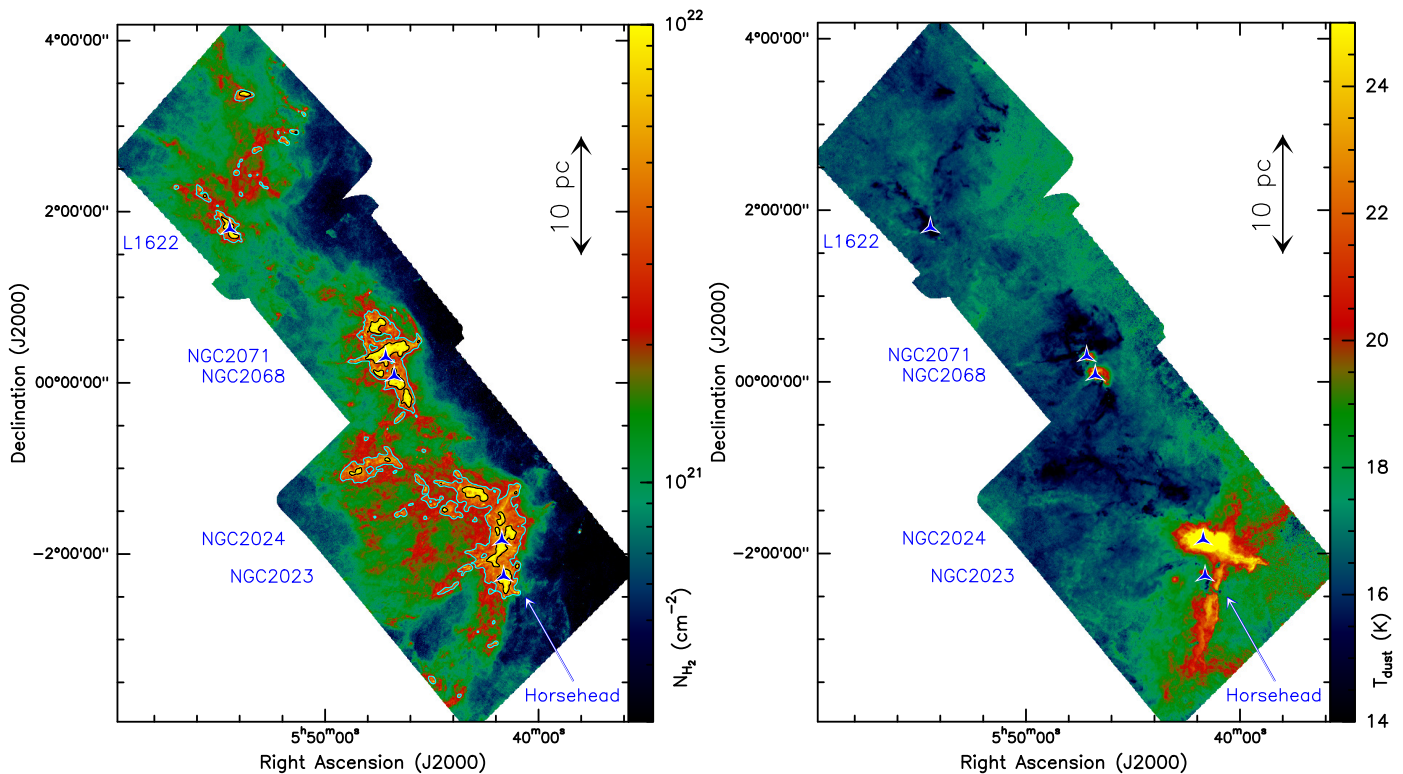


Fig. 2. *Left:* H_2 column density map of Orion B at $18.2''$ angular resolution, derived from HGBS data. The contours correspond to $A_V \sim 3$ (cyan) and 7 mag (black) in a column density map smoothed to a resolution of $2''$. *Right:* dust temperature map of the Orion B region at $36.3''$ resolution, as derived from the same data set. Blue stars mark the NGC 2023 and 2024, NGC 2068 and 2071 HII regions and reflection nebulae, and the L1622 cometary cloud. The position of the Horsehead Nebula is also shown.

e.g., Ochsendorf et al. 2015). Both the Orion A (Polychroni et al., in prep.) and the Orion B cloud (this paper) have been observed by the HGBS.

Within the Orion B cloud complex discussed in here, the most prominent features are the clumps of gas and dust associated with the NGC 2024 H II region, the NGC 2023, 2068, and 2071 reflection nebulae, and the Horsehead Nebula, as well as the Lynds 1622 cometary cloud in the north of our observed region (see Fig. 2). The cometary, trunk-like column density features and their alignments in the northern region of the field strongly suggest that L1622 – and the clouds north of it – interact with the $H\alpha$ shell of Barnard’s Loop, thus these northern clouds may also be at a closer distance of $d \sim 170\text{--}180$ pc (Bally 2008; Lallement et al. 2014), in front of the rest of Orion B. However, as the distance to Barnard’s Loop is still uncertain (see e.g., Ochsendorf et al. 2015, and references therein), for simplicity and until further studies, we adopt a uniform distance of 400 pc for deriving physical properties in the whole observed field. The cores identified in the northern area are nevertheless clearly marked in the catalogs attached to this paper.

From first-look *Herschel* GBS results in Orion B, Schneider et al. (2013) concluded that the deviation point of the column density probability density function (PDF) from a lognormal shape is not universal and may vary from cloud to cloud. The lognormal part of the PDF can be broadened by external compression, which is consistent with numerical simulations. The appearance of a power-law tail at the higher density end of the PDFs may be due to the global collapse of filaments and/or to core formation.

SCUBA-2 observations of Orion B allowed Kirk et al. (2016a) to identify and characterize ~ 900 dense cores. Their

clustering and mass segregation properties were studied by Kirk et al. (2016b) and Parker (2018). Using spatially- and spectrally-resolved observations from the IRAM-30 m telescope (Pety et al. 2017), the cloud was segmented in regions of similar properties by Bron et al. (2018) and its turbulence was characterized by Orkisz et al. (2017), who compared it with star formation properties derived from *Spitzer* and *Chandra* counts of young stellar objects (YSOs; Megeath et al. 2012, 2016).

The present paper is organized as follows. Section 2 provides details about the *Herschel* GBS observations of the Orion B region and the data reduction. Section 3 presents the dust temperature and column density maps derived from *Herschel* data, describes the filamentary structure in these maps, and explains the extraction and selection of various dense cores and their observed and derived properties. In Sect. 4, we compare the spatial distributions of cores and filaments, discuss the mass segregation of dense cores, and interpret the typical core-to-core and core-to-filament separations. We also present further observational evidence of a column density transition for prestellar core formation, along with estimates of the typical prestellar core lifetime and a comparison of the prestellar CMF in Orion B with the stellar IMF. Finally, Sect. 5 concludes the paper.

2. *Herschel* observations and data reduction

The *Herschel* Gould Belt survey observations of the Orion B complex were taken between 25 September 2010 and 13 March 2011 with the *Herschel* space observatory (Pilbratt et al. 2010). The SPIRE and PACS parallel-mode scan maps covered a common ~ 19 deg² area with both SPIRE (Griffin et al. 2010) and PACS (Poglitsch et al. 2010). With one repetition in

two orthogonal observing directions, three tiles were imaged (OBSIDs: 1342205074, 1342205075, 1342215982, 1342215983, 1342215984, 1342215985) with a scanning speed of $60''\text{s}^{-1}$. The total duration of the mapping was 19.5 hr. The above strategy is similar for all parallel-mode SPIRE and PACS observations of the HGBS.

The PACS data reduction was done with the same tools and in the same way as for the Aquila cloud (see Sect. 3 of Könyves et al. 2015). The PACS 70 and $160\mu\text{m}$ output fits files were produced in $\text{Jy}/3''$ -pixel units.

The SPIRE $250\mu\text{m}$, $350\mu\text{m}$, and $500\mu\text{m}$ data were also reduced as presented in Könyves et al. (2015) with the exception of an additional correction. The $250\mu\text{m}$ data were saturated in the course of the observations at the center of the NGC 2024 region. In order to correct for this local saturation, a small patch was re-observed in SPIRE photometer mode (OBSID: 1342239931). The re-observed stamp could not be directly mosaicked –or reduced together– with the original large map, because the edges of the small patch remained strongly imprinted in the combined map. To get around this problem, we 1) reprojected the re-observed saturation stamp to the same pixel grid as that of the original map, after which we 2) correlated the original pixel values with those of the re-observed patch in the commonly covered spot (excluding the noisy map edges of the small patch). Then, 3) this correlation was fitted with a linear relation and 4) the originally saturated pixels were assigned the linear fit-corrected values. No artifact was left in the resulting $250\mu\text{m}$ map.

The three tiles observed with both PACS and SPIRE were separately reduced, which allowed us to derive more realistic temperature and column density maps (see Sect. 3.1 below).

3. Results and analysis

3.1. Dust temperature and column density maps

The Orion B region observed with *Herschel*'s SPIRE and PACS was covered by three tiles in order to follow the elongated dense structures. The final maps (see e.g., Fig. 2) span $\sim 8^\circ$ in declination. For constructing temperature and column density maps, we decided, therefore, to add *Planck* offsets separately to these three tiles (at 160 – $500\mu\text{m}$), as the offsets may not be the same in the southern and northern ends of the maps. The derivation of the zero-level offsets for the *Herschel* maps was made as described in Bracco et al. (in prep.) from comparison with *Planck* and IRAS data (see also Bernard et al. 2010). After adding separate zero-level offsets, the three tiles at a given wavelength were then stitched together into one big mosaic. The applied offsets are listed in Table 1.

We smoothed all *Herschel* images to the resolution of the $500\mu\text{m}$ map ($36.3''$) and reprojected them to the same pixel grid. We then constructed a dust temperature (T_d) and a column density (N_{H_2}) map from pixel-by-pixel spectral energy distribution (SED) fitting using a modified blackbody function (cf. Könyves et al. 2015). As part of a standard procedure, we derived two column density maps: a “low-resolution” map at the $36.3''$ resolution of the SPIRE $500\mu\text{m}$ data and a “high-resolution” map at the $18.2''$ resolution of the SPIRE $250\mu\text{m}$ data. The detailed procedure used to construct the high-resolution column density map is described in Appendix A of Palmeirim et al. (2013). As in previous HGBS papers, we here adopt the dust opacity law, $\kappa_\lambda = 0.1 \times (\lambda/300\mu\text{m})^{-\beta} \text{cm}^2 \text{g}^{-1}$, fixing the dust emissivity index β to 2 (cf. Hildebrand 1983).

Table 1. Applied zero-level offsets in MJy sr^{-1} .

	$160\mu\text{m}$	$250\mu\text{m}$	$350\mu\text{m}$	$500\mu\text{m}$
Southern tile	67.3	60.8	32.0	13.1
Middle tile	57.9	48.4	25.8	10.8
Northern tile	53.1	51.1	27.9	11.7

Figure 2 (left and right) show the high-resolution column density map and dust temperature map, respectively, of the Orion B cloud complex. When smoothed to $36.3''$ resolution, the high-resolution column density map is consistent with the standard, low-resolution column density map. In particular, the median ratio of the two $36.3''$ resolution maps is 1 within $\pm 5\%$. We also checked the reliability of our high-resolution column density map against the *Planck* optical depth map of the region and near-infrared extinction maps. The $850\mu\text{m}$ *Planck* optical depth map was converted to an H_2 column density image using the above dust opacity law. Then, the *Herschel* and *Planck* N_{H_2} maps were compared, showing good agreement within $\pm 5\%$. This confirmed the validity and accuracy of the applied zero-level offsets.

The high-resolution N_{H_2} map was also compared to two near-infrared extinction maps. The first extinction map was derived from 2MASS data following Bontemps et al. (2010) and Schneider et al. (2011), with a FWHM spatial resolution of $\sim 120''$. The other extinction map was also made from 2MASS point-source data, using the NICEST near-infrared color excess method (Lombardi 2009, and Lombardi et al., in prep¹). For both comparisons, the *Herschel* column density map was first smoothed to the resolution of the extinction maps and converted to visual extinction units assuming $N_{\text{H}_2} (\text{cm}^{-2}) = 0.94 \times 10^{21} A_V (\text{mag})$ (Bohlin et al. 1978). We then compared the data points of the converted *Herschel* maps to those of the A_V maps on the same grid. The resulting $A_{V,\text{HGBS}}/A_{V,\text{Bontemps}}$ and $A_{V,\text{HGBS}}/A_{V,\text{Lombardi}}$ ratio maps are shown in Fig. E.1 over the field covered by Fig. 2. The median values of both ratios over the whole area are ~ 0.5 . In the extinction range $A_V = 3$ – 7 mag, the ratios are also similar, ~ 0.6 and ~ 0.5 , respectively. Both extinction maps are in good agreement with each other, while the HGBS column density map indicates lower values by a factor of < 2 . This may be the result of a combination of various factors, such as different techniques applied to the *Herschel* and 2MASS datasets, and less reliable dust opacity assumptions in low extinction regions, which are more exposed to the stronger radiation field in Orion B than in other HGBS regions (cf. Roy et al. 2014).

3.2. Filamentary structure of the Orion B cloud complex

Following André et al. (2014) and Könyves et al. (2015), we define an interstellar filament as any elongated column-density structure in the cold ISM which is significantly denser than its surroundings. We adopt a minimum aspect ratio of ~ 3 and a minimum column density excess of $\sim 10\%$ with respect to the local background, that is, $\Delta N_{\text{H}_2}^{\text{fil}}/N_{\text{H}_2}^{\text{bg}} > 0.1$, when averaged along the length of the structure.

In order to trace filaments in the *Herschel* maps and in the column density map, we used the multi-scale algorithm *getfilaments* (Men'shchikov 2013). Briefly, by analyzing highly-filtered spatial decompositions of the images across a

¹ <http://www.interstellarclouds.org/html>

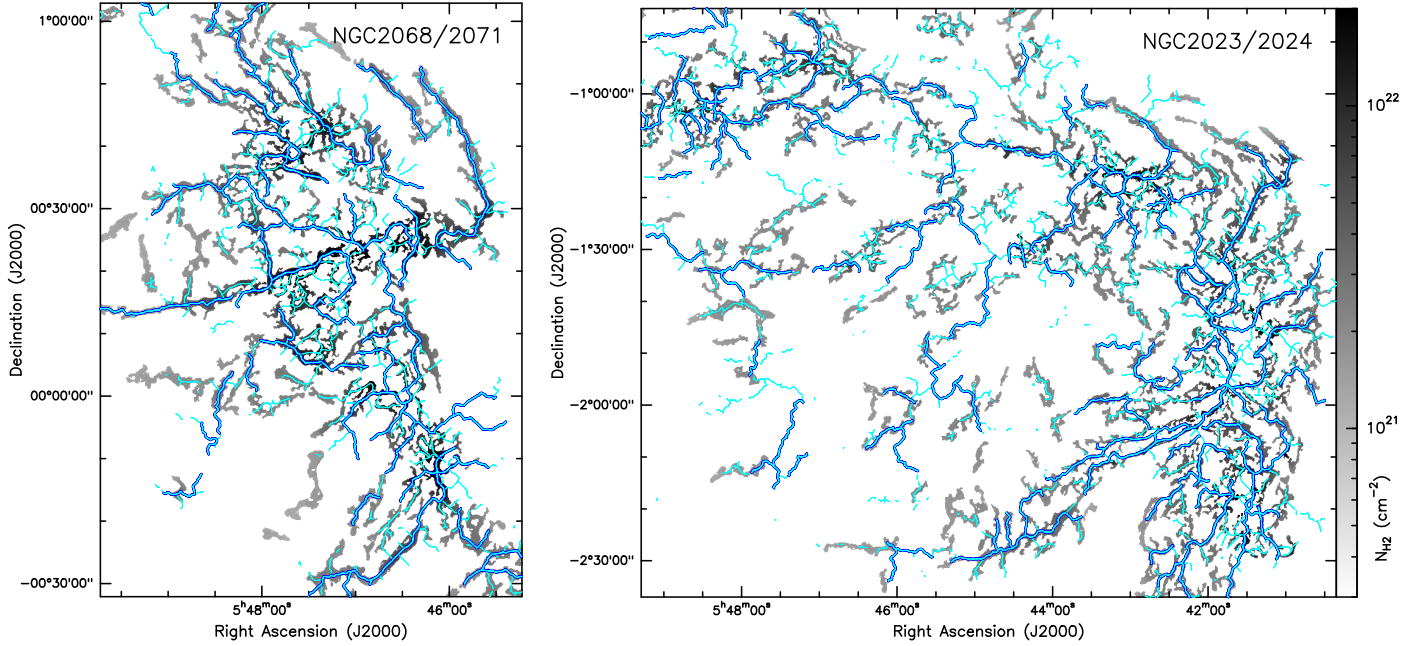


Fig. 3. Filament networks identified in the subregions NGC 2068 and 2071 (*left*), and NGC 2023 and 2024 (*right*). The gray background image displays the mask of the filamentary network traced with `getfilaments` (Men’shchikov 2013). The overlaid thick blue skeletons mark the robust filament crests identified with the DisPerSE algorithm (Sousbie 2011, see Sect. 3.2 for details). Together with the additional thin cyan crests, these filament crests make up the entire raw sample of DisPerSE filaments. Within the `getfilaments` mask, the gray scale is the same in both panels, and reflects column density values in the column density map (Fig. 2 left). Transverse angular scales up to $100''$ are shown, corresponding to ~ 0.2 pc at $d = 400$ pc. Figure E.2 (left) shows a similar view for the L1622 cloud.

wide range of scales, `getfilaments` separates elongated clusters of connected pixels (i.e., filaments) from compact sources and non-filamentary background at each spatial scale, and then constructs cumulative mask images of the filamentary structures present in the original data by accumulating the filtered signal up to an upper transverse angular scale of interest. Figures 3 and E.2 display grayscale mask images of the filamentary networks identified with `getfilaments` in the high-resolution column density maps of the NGC 2068 and 2071, NGC 2023 and 2024, and L1622. Here, we adopted an upper transverse angular scale of $100''$, or ~ 0.2 pc at $d = 400$ pc, which is consistent with the typical maximum FWHM inner width of filaments, considering a factor of ~ 2 spread around the nominal filament width of ~ 0.1 pc measured by Arzoumanian et al. (2011, 2019). The filament mask images obtained using an upper angular scale of $50''$ or ~ 0.1 pc are very similar.

As an alternative independent method, we also employed the DisPerSE algorithm (Sousbie 2011), which traces filaments by connecting saddle points to local maxima with integral lines following the gradient in a map. The filament skeletons overlaid in blue in Figs. 3 and E.2 (left) were obtained with the DisPerSE method. DisPerSE was run on the standard column density map (at $36.3''$ resolution) with $3''$ pixel $^{-1}$ scale, using a “persistence” threshold of 10^{20} cm $^{-2}$, roughly corresponding to the lowest rms level of background fluctuations in the map, and a maximum assembling angle of 50° , as recommended by Arzoumanian et al. (2019). This led to a raw sample of DisPerSE filaments. Then, to select a robust sample of filaments, raw filamentary structures were trimmed below the peak of the column density PDF (see Fig. 4 left), and raw features shorter than $10\times$ the HPBW resolution of the map were removed, as suggested by Arzoumanian et al. (2019). The resulting sample of robust DisPerSE filaments comprises a total of 238 crests shown as thick blue skeletons

in Figs. 3 and E.2 (left). The thin cyan crests show the additional, more tentative filaments from the raw sample extracted with DisPerSE.

Although we shall see in the following that physical results derived from either of the two methods are similar, DisPerSE tends to trace longer filamentary structures as a result of its assembling step, while `getfilaments` typically finds shorter structures down to the selected spatial scales.

3.3. Distribution of mass in the Orion B complex

The probability density function of column density in the Orion B cloud is shown in Fig. 4 (left). For a similar N_{H_2} -PDF plot from an earlier column density map of Orion B based on HGBS data, see Schneider et al. (2013).

Throughout the paper we take advantage of the Bohlin et al. (1978) conversion factor (see Sect. 3.1) according to which H_2 column density values in units of 10^{21} cm $^{-2}$ approximately correspond to A_V in magnitudes. In our terminology we use the following column density ranges in corresponding visual extinction: “low” for $A_V < 3$, “intermediate” for $A_V = 3 - 7$, and “high” for $A_V > 7$ mag, which are similar to, but not exactly the same as, those defined by Pety et al. (2017).

The column density PDF in Fig. 4 (left) is well fitted by a log-normal distribution at low column densities and by a power-law distribution above the corresponding visual extinction of $A_V \sim 3$ mag. In the left panel of Fig. 4, the lowest closed contour in the column density map (Fig. 2 left) is marked by a vertical dashed line at $A_V \sim 1$. According to Alves et al. (2017), the lowest closed contour corresponds to the completeness level of a column density PDF, down to which the PDF is generally well represented by a pure power-law. Here, above the completeness level at $A_V \sim 1$, the column density PDF is best fit by a

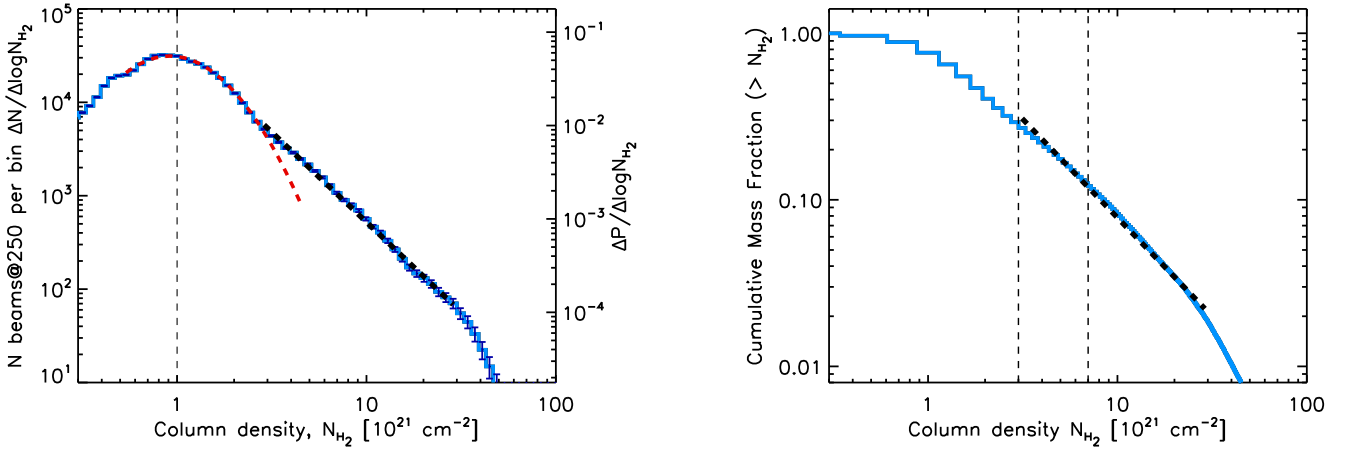


Fig. 4. *Left:* high-resolution N_{H_2} column density PDF of Orion B, derived from the column density map of Fig. 2 left. The lognormal fit (dashed red curve) peaks at $0.92 \times 10^{21} \text{ cm}^{-2}$ in N_{H_2} , and has a standard deviation of ~ 0.25 in $\log_{10} N_{\text{H}_2}$. The power-law fit to the higher column density tail at $A_V \gtrsim 3$ (dashed black line) is $\Delta N / \Delta \log N_{\text{H}_2} \propto N_{\text{H}_2}^{-1.9 \pm 0.2}$. The vertical dashed line at $A_V \sim 1$ marks the lowest closed contour in the column density map. *Right:* corresponding (normalized) cumulative mass fraction as a function of column density. The dense material above $A_V \sim 3$ – 7 mag represents only ~ 30 – 13% of the total cloud mass, respectively, as indicated by the two dashed vertical lines. A power-law fit to the cumulative mass fraction for $A_V \gtrsim 3$ gives $M(> N_{\text{H}_2}) \propto N_{\text{H}_2}^{-1.1 \pm 0.2}$.

power-law plus a lognormal. Although the break between the two fits at $A_V \sim 3$ is not very pronounced, the column density excess in the lognormal part above the power-law fit appears to be significant.

The power-law tail of the PDF is as developed as in the case of the Aquila cloud complex (Könyves et al. 2015). In Orion B, however, the best power-law fit for $A_V > 3$ corresponds to $\Delta N / \Delta \log N_{\text{H}_2} \propto N_{\text{H}_2}^{-1.9 \pm 0.2}$, which is significantly shallower than the logarithmic slope of -2.9 ± 0.1 found in the Aquila cloud.

The total mass of the Orion B clouds was derived from the column density map in Fig. 2 (left) as:

$$M_{\text{cl}} = \delta A_{\text{pixel}} \mu_{\text{H}_2} m_{\text{H}} \sum_{\text{pixels}} N_{\text{H}_2}.$$

In the above equation, δA_{pixel} is the surface area of one pixel at the adopted distance ($d = 400$ pc), $\mu_{\text{H}_2} = 2.8$ is the mean molecular weight per H_2 molecule, m_{H} is the hydrogen atom mass, and the sum of column density values is over all of the pixels in the map. This approach yielded a total cloud mass of $\sim 2.8 \times 10^4 M_{\odot}$.

In order to obtain the cumulative mass fraction of gas mass as a function of column density (Fig. 4 right), we repeated the above mass calculation for the pixels above a given column density. The dense molecular gas material represents only $\sim 13\%$ ($\sim 3.7 \times 10^3 M_{\odot}$) of the total cloud mass above a visual extinction $A_V \sim 7$ mag. As in other clouds, the low and intermediate column density regions at $A_V < 3$ – 7 mag in the map of Fig. 2 (left) occupy most ($>95\%$) of the surface area imaged with *Herschel* and account for most (~ 74 – 88%) of the cloud mass.

In agreement with the typical ratios $A_{V,\text{HGBS}}/A_{V,\text{ext}} \gtrsim 0.5$ found in Sect. 3.1 from comparing the HGBS column density map with extinction maps, we note that the total mass reported here for the Orion B clouds is a factor of ~ 1.8 lower than the total mass indicated by the extinction maps ($\sim 5 \times 10^4 M_{\odot}$).

3.4. Multiwavelength core extraction with getsources

Compact sources were extracted simultaneously from the PACS and SPIRE images with the getsources algorithm

(Men’shchikov et al. 2012)². A complete summary of the source extraction method can be found in Sect. 4.4 of Könyves et al. (2015), and full technical details are provided in Men’shchikov et al. (2012). Briefly, the extraction process consists of a detection and a measurement stage. At the detection stage, getsources analyzes fine spatial decompositions of all the observed wavebands over a wide range of scales. This decomposition filters out irrelevant spatial scales and improves source detectability, especially in crowded regions and for extended sources. The multi-wavelength design combines data over all wavebands and produces a wavelength-independent detection catalog. At the measurement stage, properties of detected sources are measured in the original observed images at each wavelength.

For the production of HGBS first-generation catalogs of starless and protostellar cores, two sets of dedicated getsources extractions are performed, optimized for the detection of dense cores and YSOs/protostars, respectively. In the first, “core” set of extractions, all of the *Herschel* data tracing column density are combined at the detection stage, to improve the detectability of dense cores. The detection image is thus combined from the 160, 250, 350, and 500 μm maps, together with the high-resolution column density image (see Sect. 3.1) used as an additional “wavelength”. The 160 μm component of the detection image is “temperature-corrected” to reduce the effects of strong, anisotropic temperature gradients present in parts of the observed fields (see Könyves et al. 2015, for details).

A second, “protostellar” set of getsources extractions is performed to trace the presence of self-luminous YSOs/protostars and discriminate between protostellar and starless cores. In this second set of extractions, the only *Herschel* data used at the detection stage are the PACS 70 μm data. This allows us to exploit the result that the level of point-like 70 μm emission traces the internal luminosity (and therefore the presence) of a protostar very well (e.g., Dunham et al. 2008).

² The HGBS first-generation catalog of cores presented in this paper (see Appendix A) was produced with the “November 2013” major release of getsources (v1.140127), which is publicly available from <http://gouldbelt-herschel.cea.fr/getsources>.

At the measurement stage of both sets of extractions, source properties are measured at the detected positions of either dense cores or YSOs/protostars, using the observed, background-subtracted, and deblended images at all five *Herschel* wavelengths, plus the high-resolution column density map. The only difference from the procedure described in Könyves et al. (2015) is that, following improvements in the preparation of maps for source extraction, a new method of background flattening, called `getimages` (Men'shchikov 2017), was used before performing the protostellar set of `getsources` extractions. Tests have shown that this additional step drastically reduces the large number of spurious $70\ \mu\text{m}$ sources in areas of bright, structured PDR (photodissociation region) emission around HII regions. Before extracting protostellar sources, `getimages` subtracts the large-scale background emission and equalizes the levels of small-scale background fluctuations in the images using a median-filtering approach.

3.5. Selection and classification of reliable core detections

3.5.1. Initial core selection

The criteria used to select reliable dense cores and YSOs from the raw source catalogs delivered by `getsources` are described in detail in Sect. 4.5 of Könyves et al. (2015).

First we select candidate dense cores (starless and protostellar) from the “core” extractions using criteria based on several output parameters provided by `getsources`: detection significance, signal-to-noise ratio (S/N), and “goodness” parameter. Then, we select candidate YSOs from the second set of extractions based on their corresponding detection significance, S/N, flux density, goodness, and source size and elongation parameters.

Afterward, we cross-match the selected dense cores with the candidate YSOs/protostars and distinguish between starless cores and young (proto)stellar objects based on the absence or presence of compact $70\ \mu\text{m}$ emission. YSOs must be detected as compact emission sources above the 5σ level at $70\ \mu\text{m}$, while starless cores must remain undetected in emission (or detected in absorption) at $70\ \mu\text{m}$ (Könyves et al. 2010).

In addition to Aquila (Könyves et al. 2015), this whole method has been so far applied to studies of various regions of the HGBS: the Taurus L1495 cloud (Marsh et al. 2016), Corona Australis (Bresnahan et al. 2018), the Lupus complex (Benedettini et al. 2018), Perseus (Pezzuto et al. 2019), Ophiuchus (Ladjelate et al. 2019), the Cepheus Flare (Di Francesco et al., in prep.), further parts of Taurus (Kirk et al., in prep.), and the Orion A clouds (Polychroni et al., in prep.).

3.5.2. Post-selection checks

All of the candidate cores initially selected using the criteria defined in detail in Sect. 4.5 of Könyves et al. (2015) were subsequently run through an automated post-selection step. Given the large number (~ 2000) of compact sources detected with *Herschel* in the Orion B region, we tried to define automatic post-selection criteria based on source morphology in the SPIRE and PACS and column density images (see blow-up maps in Figs. A.1 and A.2), in order to bypass the need for detailed visual inspection. A final visual check of all candidate cores in the present catalog (Table A.1) was nevertheless performed. With our automated post-selection script described in detail in Appendix B, we revisited the location of each formerly selected core in all of the *Herschel* maps (including the column density plane) and

performed a number of pixel value checks within and around the core's FWHM contour to make sure that it corresponds to a true intensity peak or enhancement in the analyzed maps. This post-selection procedure allowed us to remove dubious sources from the final catalog of cores in Table A.1.

To eliminate extragalactic contaminants from our scientific discussion, we cross-matched all selected sources with the NASA Extragalactic Database³ (NED). We found matches within $6''$ for four classified external galaxies, which were removed from our scientific analysis. As Orion B lies toward the outer Galaxy and below the Galactic plane, we can expect several extragalactic contaminants in the low column density portions of the field, beyond the four sources listed in the NED database. Using *Herschel*'s SPIRE data from the HerMES extragalactic survey (Oliver et al. 2012), Oliver et al. (2010) determined that the surface number density of extragalactic sources at the level $S_{250\ \mu\text{m}} = 100\ \text{mJy}$ is about $12.8 \pm 3.5\ \text{deg}^{-2}$. In the $\sim 19\ \text{deg}^2$ area observed with *Herschel* in Orion B, our catalog includes three candidate cores with $250\ \mu\text{m}$ integrated flux densities below $100\ \text{mJy}$ and 26 candidate cores with $250\ \mu\text{m}$ integrated flux densities below $200\ \text{mJy}$, mostly in low background emission spots. Roughly 1/3 of these candidate cores with low flux densities at $250\ \mu\text{m}$ have Unclassified Extragalactic Candidate matches within $6''$. These 26 tentative cores are listed in our observed core catalog (Table A.1), but excluded from the scientific analysis.

Likewise, we checked likely associations between the selected *Herschel* cores and objects in the SIMBAD database or the *Spitzer* database of Orion B by Megeath et al. (2012). Any match is reported in the catalog of Table A.1. In particular, 30 associations with a *Spitzer* source were found using a $6''$ matching radius, where we used the same selection of YSOs from Megeath et al. (2012) as Shimajiri et al. (2017).

Overall, our `getsources` selection and classification procedure resulted in a final sample of 1844 dense cores in Orion B (not counting ~ 26 possible extragalactic contaminants), comprising 1768 starless cores and 76 protostellar cores (see Fig. 5). The observed properties of all these post-selected *Herschel* cores are given in the accompanying online catalog with a few example lines in Table A.1. The corresponding derived properties of the 1844 dense cores are provided in Table A.2.

3.6. Derived core properties

For deriving core physical properties we used a SED fitting procedure similar to that described in Sect. 3.1 for the production of the column density map. The SED data points for the properties of each core were given by their integrated flux densities measured by `getsources`, and the data points were weighted by $1/\sigma_{\text{err}}^2$, where σ_{err} is the flux measurement error estimated by `getsources` for each data point. The modified blackbody fits of the observed SEDs were obtained in IDL with the MPCURVEFIT routine (Markwardt 2009). These fits provided direct mass and line-of-sight-averaged dust temperature estimates for most of the selected cores. We derived core masses with the same dust opacity assumptions as in Sect. 3.1 and a distance $d = 400\ \text{pc}$ for Orion B. The angular FWHM size estimates, measured by `getsources` at $18.2''$ resolution in the high-resolution column density map, were converted to a physical core radius. In our catalog (see Table A.2), we provide estimates for both the deconvolved and the observed radius of

³ <https://ned.ipac.caltech.edu/forms/nearposn.html>

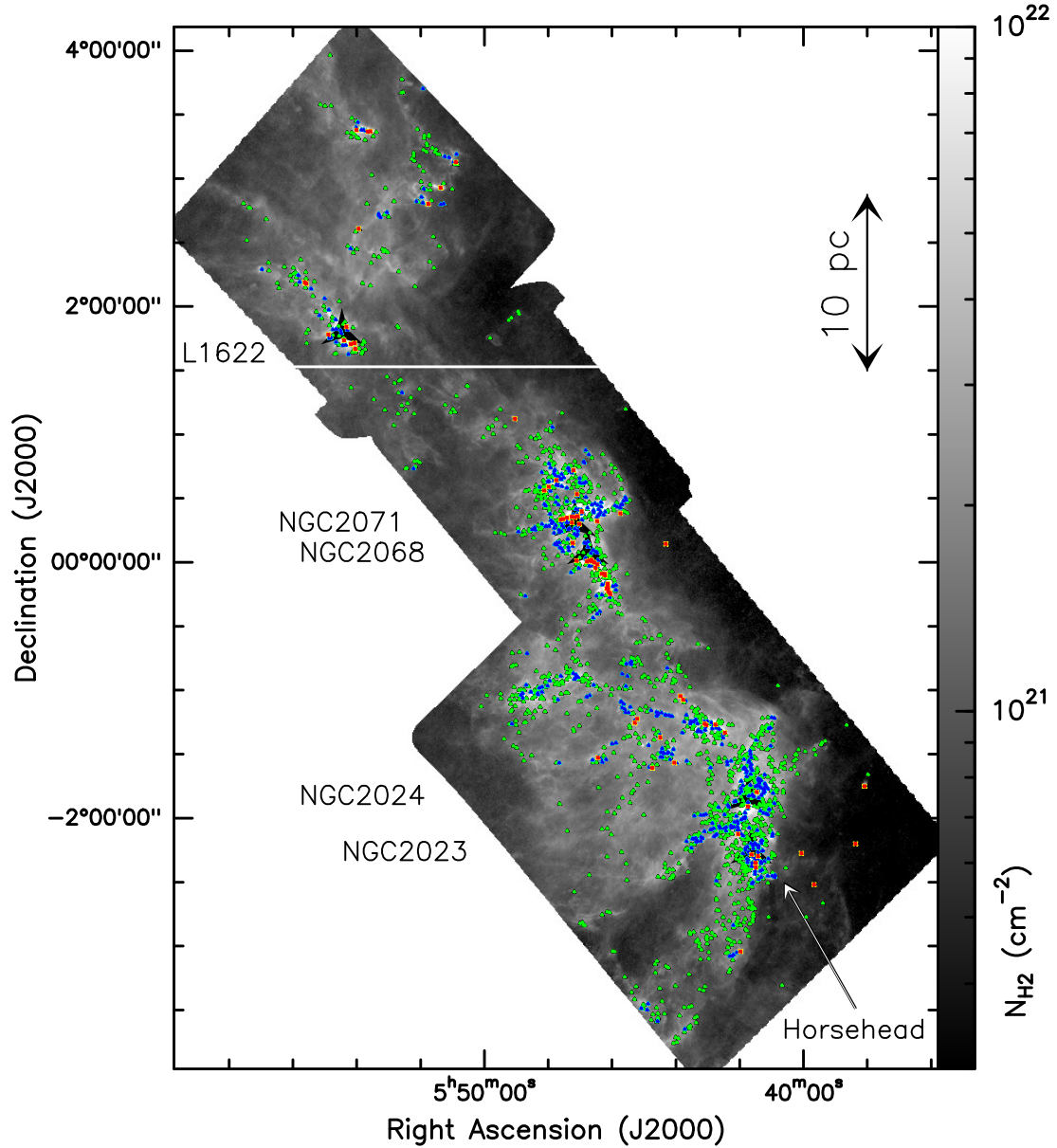


Fig. 5. High-resolution ($\sim 18''$) column density map of Orion B, derived from SPIRE and PACS observations. The positions of the 1768 identified starless cores (green triangles), 490 *robust* prestellar cores (blue triangles), and 76 embedded protostellar cores (red symbols) are overplotted. The vast majority of the cores lie in high column density areas. The white declination line at $\text{Dec}_{2000} = 1^{\circ}31'55''$ marks the lower boundary of the northern region where cores may be associated with the Barnard’s Loop and at a more uncertain distance ($d \sim 170\text{--}400$ pc). See Sects. 1 and 3.5.2 for details.

each core (estimated as the geometrical average between the major and minor FWHM sizes).

For each core, the peak (or central beam) column density, average column density, central-beam volume density, and the average volume density were then derived based on their mass and radius estimates (see Sect. 4.6. in Könyves et al. 2015). The column- and volume density distributions for the different population of cores are shown in Fig. 6. In Table A.2, all the above derived properties are provided for the whole sample of selected *Herschel* cores.

In order to assess the robustness of our SED fits for each source, we compared two successive runs of the fitting procedure with somewhat different weighting schemes. In the first run the *getsources* detection errors were used to weigh the SED points and the $70\ \mu\text{m}$ data were included in the fit, while

the more conservative measurement errors were used without fitting the $70\ \mu\text{m}$ data points in the second run. The following criteria were applied for accepting the SED fits for a given source: (1) significant flux measurements exist in at least three *Herschel* bands, (2) the source has larger integrated flux density at $350\ \mu\text{m}$ than at $500\ \mu\text{m}$, and (3) less than a factor of 2 difference is found between the core mass estimates from the two SED fits.

The starless core masses with rejected SED fit results from the above procedure were estimated directly from the measured integrated flux density at the longest significant wavelength. Optically thin dust emission was assumed at the median dust temperature that we found for starless cores with reliable SED fits. Such cores have more uncertain properties for which we assigned a “no SED fit” comment in Table A.2.

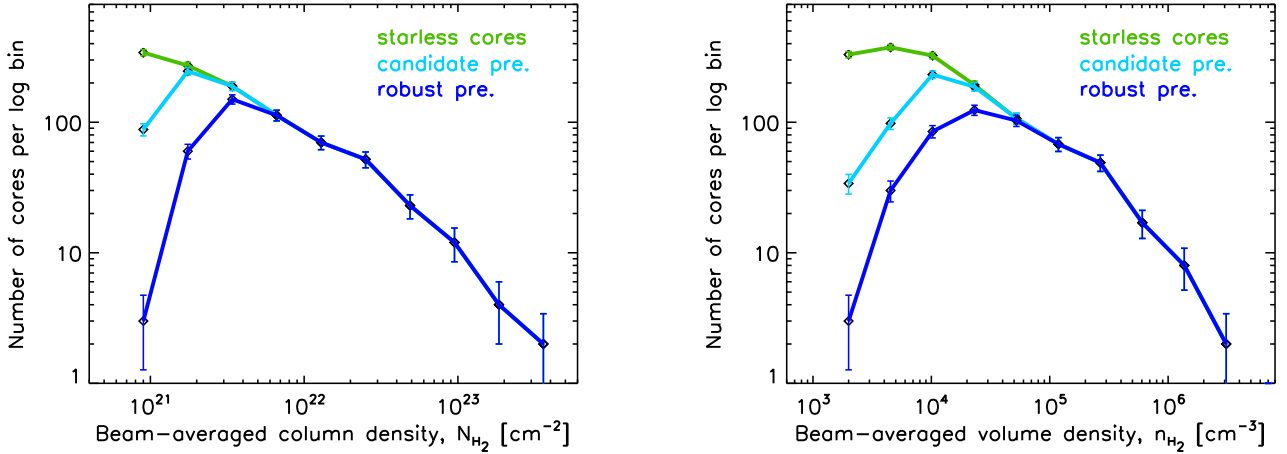


Fig. 6. Distributions of beam-averaged column densities (*left*) and beam-averaged volume densities (*right*) at resolution of SPIRE 500 μm observations for 1768 starless cores (green), 804 *candidate* prestellar cores (light blue), and 490 *robust* prestellar cores (dark blue curve) in Orion B.

The accuracy of our core mass estimates is affected by two systematic effects: (1) uncertainties in the dust opacity law induce mass uncertainties of up to a factor $\sim 1.5\text{--}2$ (cf. Roy et al. 2014), (2) the SED fits only provide line-of-sight averaged dust temperatures. In reality, however, starless cores are externally heated objects, and they can show a significant drop in dust temperature toward their centers (e.g., Nielbock et al. 2012; Roy et al. 2014). The mass of a starless core may be underestimated in such a situation, as the average SED temperature may overestimate the mass-averaged dust temperature. For low column density cores, such as B68 (Roy et al. 2014), this effect is less than $\sim 20\%$, but for high-density cores, with average column densities above $\sim 10^{23} \text{ cm}^{-2}$, it increases to up to a factor of ~ 2 . Here, we did not attempt to use special techniques (cf. Roy et al. 2014; Marsh et al. 2014) to retrieve the intrinsic temperature structure and derive more accurate mass estimates.

The Monte-Carlo simulations that we used to estimate the completeness of the survey (see Sect. 3.8 below), however show that the SED masses of starless cores (in Table A.2) are likely underestimated by only $\sim 25\%$ on average compared to the intrinsic core masses. This is mainly because the SED dust temperatures slightly overestimate the intrinsic mass-averaged temperatures within starless cores. We have not corrected the column- and volume densities in Table A.2 and in Fig. 6 for this small effect.

We may also compare the results of the present core census with the SCUBA-2 findings of Kirk et al. (2016a), used in both Kirk et al. (2016b) and Parker (2018). Adopting a matching separation of $<6''$, we found 192 matches between HGBS starless cores and SCUBA-2 cores and 47 matches between HGBS protostellar cores and SCUBA-2 objects. The relatively low number of matches is the result of the significantly smaller area coverage of the SCUBA-2 data, the higher sensitivity and broader wavelength coverage of the *Herschel* data, and very different source-extraction techniques. As the assumptions about dust emissivity properties differ in the HGBS and SCUBA-2 studies, we re-derived two sets of mass estimates for the SCUBA-2 cores from the published 850 μm total fluxes: (1) the first set of mass estimates ($M_{\text{SCUBA-2,Td}}$) was derived using the standard HGBS dust opacity law (see Sect. 3.1) and the dust temperatures estimated from *Herschel* SED fitting ($T_{\text{d}}^{\text{SED}}$); (2) the second set ($M_{\text{SCUBA-2,20K}}$) was derived using the same HGBS dust opacity law and a uniform dust temperature of 20 K for all cores (as assumed by Kirk et al. 2016a). The resulting comparison

of core mass estimates is summarized in Fig. E.3, which plots the distributions of the ratios $M_{\text{SCUBA-2,Td}}/M_{\text{HGBS}}$ and $M_{\text{SCUBA-2,20K}}/M_{\text{HGBS}}$ for all SCUBA-2–HGBS core matches, separately for starless and protostellar cores. In each panel of Fig. E.3, the corresponding median ratio is indicated by a red dashed line. Overall, a good correlation exists between the re-derived SCUBA-2 masses and the HGBS masses. The $M_{\text{SCUBA-2,Td}}$ mass estimates for the matched starless cores are typically only $\sim 25\%$ higher, and the $M_{\text{SCUBA-2,20K}}$ estimates $\sim 60\%$ lower, than the M_{HGBS} masses. The most likely reason for the relatively low $M_{\text{SCUBA-2,20K}}/M_{\text{HGBS}}$ ratios is that the typical dust temperature of starless cores is significantly lower than 20 K, implying that $M_{\text{SCUBA-2,20K}}$ typically underestimates the true mass of a starless core. For the 47 matched protostellar cores, the $M_{\text{SCUBA-2,20K}}/M_{\text{HGBS}}$ ratio is close to 1 on average, indicating a very good agreement between the $M_{\text{SCUBA-2,20K}}$ and M_{HGBS} mass estimates, while the $M_{\text{SCUBA-2,Td}}$ masses are typically a factor of ~ 2 higher than the M_{HGBS} masses. The latter trend most likely arises from the fact that the dust temperature $T_{\text{d}}^{\text{SED}}$, derived from our standard SED fitting between 160 and 500 μm , typically overestimates the “mass-averaged” temperature of a protostellar core. We stress, however, that $T_{\text{d}}^{\text{SED}}$ is more reliable for starless cores and that protostellar cores are not the main focus of the present paper.

3.7. Selecting self-gravitating prestellar cores

The subset of starless cores which are self-gravitating are likely to evolve to protostars in the future and can be classified as *prestellar* cores (cf. Ward-Thompson et al. 2007). In the absence of spectroscopic observations for most of the *Herschel* cores, the self-gravitating status of a core can be assessed using the Bonnor–Ebert (BE) mass ratio $\alpha_{\text{BE}} = M_{\text{BE,crit}}/M_{\text{obs}}$, where M_{obs} is the core mass as derived from *Herschel* data and $M_{\text{BE,crit}}$ is the thermal value of the critical BE mass. The first criterion adopted here to select self-gravitating cores is $\alpha_{\text{BE}} \leq 2$. This simplified approach, using the thermal BE mass and thus neglecting the nonthermal component of the velocity dispersion, is justified by observations of nearby cores in dense gas tracers (e.g., Myers 1983; Tafalla et al. 2002; André et al. 2007). These studies show that the thermal component dominates at least in the case of low-mass cores. The thermal BE mass (M_{BE}) was estimated for each object from the deconvolved core radius (R_{deconv}) that we measured in the high-resolution column density map

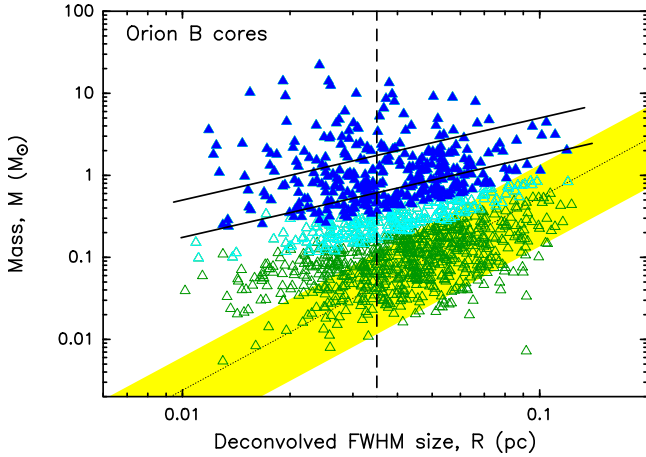


Fig. 7. Mass versus size diagram for all 1768 starless cores (triangles) identified with *Herschel* in Orion B, including the 804 *candidate* prestellar cores (light or dark blue triangles) and 490 *robust* prestellar cores (filled triangles in dark blue). The core FWHM sizes were measured with *getsources* in the high-resolution column density map (Fig. 2 left) and deconvolved from an 18.2'' (*HPBW*) Gaussian beam. The corresponding physical *HPBW* resolution at $d = 400$ pc is marked by the vertical dashed line. Models of critical isothermal Bonnor–Ebert spheres at $T = 7$ K and $T = 20$ K are plotted as black solid lines for comparison. The diagonal dotted line and yellow band display the observed mass-size correlation of diffuse CO clumps (Elmegreen & Falgarone 1996).

(see Sect. 3.6) assuming 10 K as a typical internal core temperature⁴. This selection of self-gravitating cores is illustrated in the mass versus size diagram of Fig. 7, where source positions can be used to distinguish between *robust* prestellar cores (filled blue triangles) and unbound starless cores (open green triangles).

In addition, a second, less restrictive selection of *candidate* prestellar cores (open light blue triangles in Fig. 7) was obtained by deriving an empirical lower envelope for self-gravitating objects in the mass versus size diagram, based on the Monte-Carlo simulations used in Sect. 3.8 to derive the completeness of the survey. The advantage of this less restrictive selection criterion, also employed by Könyves et al. (2015) in the Aquila cloud, is that it provides a larger, more complete sample of *candidate* prestellar cores (at the cost of including a larger fraction of misclassified unbound cores).

Here, the resulting final number of *robust* prestellar cores based on the first criterion ($\alpha_{BE} \leq 2$) was 490, and the number of *candidate* prestellar cores based on the empirical criterion was 804, out of a grand total of 1768 starless cores in the entire Orion B field. The spatial distribution of all starless cores and *robust* prestellar cores is plotted in Fig. 5. We note that all of the *robust* prestellar cores belong to the wider sample of *candidate* prestellar cores.

These two samples of prestellar cores reflect the uncertainties in the classification of gravitationally bound/unbound objects, which are fairly large for unresolved or marginally-resolved

⁴ We adopt the same typical internal core temperature of 10 K in Orion B as in the Aquila cloud (cf. Sect. 4.7 of Könyves et al. 2015) since the dust temperature maps derived from *Herschel* data suggest that the average radiation field is similar in both cloud complexes, with the possible exception of the vicinity of the bright HII region NGC 2024 (see Table 6 of Shimajiri et al. 2017). We also stress that radiative transfer models suggest that the internal temperature of starless dense cores depends only weakly on the ambient radiation field, in contrast to the temperature of the core outer layers.

cores, as the intrinsic core radius (and therefore the intrinsic BE mass) is more uncertain for such cores. In the following discussion (Sect. 4) below, we consider both samples of prestellar cores. The 314 *candidate* prestellar cores which are not *robust* are clearly marked with a “tentative bound” comment in Table A.2.

In the northern region around L1622, which may be associated with Barnard’s Loop, there are 179 starless cores ($\sim 10\%$ of the whole sample of starless cores), including 67 *candidate* prestellar cores (or $\sim 8\%$ of all *candidate* prestellar cores), 41 *robust* prestellar cores ($\sim 8\%$), and 15 protostellar cores ($\sim 20\%$ of all protostellar cores). As mentioned in Sect. 1, these cores are at a more uncertain distance. By default and for simplicity, these northern objects are assumed to be at the same distance of 400 pc as the rest of the cores (cf. Ochsendorf et al. 2015). The cores lying north of the declination line $\text{Dec}_{2000} = 1^{\circ}31'55''$ in Fig. 5 are nevertheless marked with an “N region” comment in the catalogs available at the CDS (Tables A.1 and A.2).

In the mass versus size diagram of Fig. 7 for the entire population of starless cores, there is a spread of deconvolved sizes (*FWHM*) between ~ 0.01 pc and ~ 0.1 pc and a range of core masses between $\sim 0.02 M_{\odot}$ and $\sim 20 M_{\odot}$. The fraction of self-gravitating starless objects is $\sim 28\%$ or $\sim 45\%$ considering the samples of *robust* or *candidate* prestellar cores, respectively. Most of the unbound starless cores identified with *Herschel* in Orion B are located in the same area of the mass vs. size diagram as typical CO clumps (marked by the yellow band in Fig. 7), which are known to be mostly unbound structures (e.g., Elmegreen & Falgarone 1996; Kramer et al. 1998). It can also be seen in Fig. 7 that self-gravitating prestellar cores are typically more than an order of magnitude denser than unbound CO clumps.

Finally, we note that the distributions of beam-averaged column densities and volume densities for starless cores, *candidate* prestellar cores, and *robust* prestellar cores all merge at high (column) densities in Fig. 6, suggesting that all *Herschel* starless cores with $N_{\text{H}_2}^{\text{peak}} \geq 7 \times 10^{21} \text{ cm}^{-2}$ or $n_{\text{H}_2}^{\text{peak}} \geq 4 \times 10^4 \text{ cm}^{-3}$ are dense enough and sufficiently strongly centrally concentrated to be self-gravitating and prestellar in nature.

3.8. Completeness of the prestellar core survey

Following the Monte-Carlo procedure used by Könyves et al. (2015) to estimate the completeness limit of the HGBS prestellar core census in the Aquila cloud, we performed similar simulations in Orion B. A population of 711 model Bonnor–Ebert-like cores were inserted in clean-background images at the *Herschel* wavelengths, from which we also derived a synthetic column density plane as described in Sect. 3.1. Then, core extractions were performed on the resulting synthetic images with *getsources* in the same way as for the observed data (see Sect. 3.4). The results of these simulations suggest that our sample of *candidate* prestellar cores in Orion B is $>80\%$ complete above a *true* core mass of $\sim 0.5 M_{\odot}$ (cf. Fig. 8), which translates to $\sim 0.4 M_{\odot}$ in *observed* core mass. Indeed, the observed masses of starless cores tend to be underestimated by $\sim 25\%$ due to their internal temperature gradient (see Fig. C.1–left and Appendix C for further details).

In Appendix B of Könyves et al. (2015) it was shown that the completeness level of a census of prestellar cores such as the present survey is background dependent, namely that the completeness level decreases as background cloud column density and cirrus noise increase. A similar model adapted to the case of Orion B quantifies this trend (see Fig. C.4) and shows that the

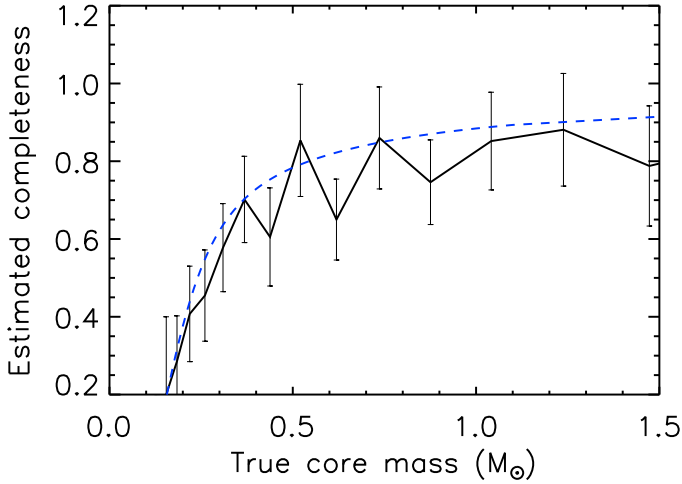


Fig. 8. Completeness curve of *candidate* prestellar cores as function of true core mass (solid line), which was estimated from Monte–Carlo simulations (see Sect. 3.8). For comparison, the global completeness curve of the model introduced at the end of Appendix C is shown by the dashed blue line.

global completeness of the present census of prestellar cores is consistent with that inferred from the Monte–Carlo simulations (see Fig. 8 and Appendix C).

4. Discussion

4.1. Spatial distribution of dense cores

4.1.1. Connection between dense cores and filaments

As already pointed out in earlier HGBS papers (e.g., André et al. 2010; Könyves et al. 2015; Marsh et al. 2016; Bresnahan et al. 2018), there is a very close correspondence between the spatial distribution of compact dense cores and the networks of filaments identified in the *Herschel* column density maps of the Gould Belt regions. Furthermore, prestellar cores and embedded protostars are preferentially found within the densest filaments with transcritical or supercritical masses per unit length (i.e., $M_{\text{line}} \gtrsim M_{\text{line,crit}} \equiv 2 c_s^2/G$) (e.g., André et al. 2010, 2014).

The two panels of Fig. 9 provide close-up views of two subfields of Orion B, where the projected locations of *robust* prestellar cores are overlaid on the filament masks (shown up to $100''$ transverse angular scales) extracted with `getfilaments` (see Sect. 3.2). More than 80% of the *robust* prestellar cores are found inside this filament sample in the whole Orion B region. The connection between cores and filaments can be quantified in more detail based on the census of cores presented in Sects. 3.4, 3.5, and 3.7 and the census of filaments described in Sect. 3.2. The locations of extracted cores were correlated with various filament samples to illustrate the robustness of this connection. We consider three of these filament samples, also displayed in Fig. 3:

- `getfilaments` mask images including transverse angular scales up to $50''$ or $100''$, which correspond to transverse physical scales up to ~ 0.1 pc or ~ 0.2 pc at $d = 400$ pc. Such $100''$ mask images are shown in grayscale in, for example, Fig. 3.
- Maps of robust filament crests extracted with the DisPerSE algorithm and cleaned with the criteria described in Sect. 3.2 (thick blue skeletons overplotted in Fig. 3). Corresponding mask images were prepared from the 1-pixel-wide

crests using Gaussian smoothing kernels with three different FWHM widths: 0.05 pc, 0.1 pc, and 0.2 pc.

- Maps of raw filament crests extracted with the DisPerSE algorithm, prior to cleaning and post-selection (see Sect. 3.2). In Fig. 3, the combination of blue and cyan filament crests together make up the DisPerSE raw sample. As for DisPerSE robust crests, mask images were prepared using three Gaussian smoothing kernels with FWHMs of 0.05 pc, 0.1 pc, and 0.2 pc.

Table 2 reports the fractions of cores lying within the footprints of each of the above-mentioned filament samples, assuming that the intrinsic inner width of each filament is within a factor of 2 of the typical 0.1 pc value found by Arzoumanian et al. (2011, 2019) in nearby clouds, including Orion B.

We also derived the distribution of core separations to the nearest filament crests using various core samples (starless, *candidate* and *robust* prestellar) and the crests of both the robust and the raw sample of DisPerSE filaments. The results shown in Fig. 10 were obtained with the raw (uncleaned) sample of DisPerSE filaments. The median separation to the nearest filament is 0.006 pc for the *robust* (dark blue histogram) and *candidate* (light blue) prestellar core samples, and 0.007 pc for the starless core sample (green).

The fraction of cores within the nominal filament width (0.1 pc) of the raw DisPerSE sample, marked by the red vertical line in Fig. 10, is also presented in Table 2. Based on the numbers given in Table 2, we confirm that a high fraction of prestellar cores are closely associated with filaments in Orion B, as already observed in Aquila (Könyves et al. 2015), Taurus L1495 (Marsh et al. 2016), and Corona Australis (Bresnahan et al. 2018), for example.

The tight connection between cores and filaments is found independently of the detailed algorithm employed to trace filamentary structures (see Table 2). In particular, while one may think that the association between cores and filaments is partly an artificial consequence of the way DisPerSE constructs filament crests (by joining saddle points to local maxima), we stress that the same connection is seen when using `getfilaments` to determine filament footprints completely independently of column density maxima (see Sect. 3.2).

When the DisPerSE raw samples of filaments are considered (which are the most complete samples of elongated structures used in Table 2), the distributions show that most ($\gtrsim 90\%$) starless or prestellar dense cores lie very close to identified filamentary structures. This suggests that the earliest phases of star formation are necessarily embedded in elongated structures (of any density), which may provide an optimal basis for cores to gain mass from their immediate environment. Such an increase in the number of cores residing in filaments when considering a more complete filament sample is also found in the Aquila cloud.

4.1.2. Nearest neighbor core separation

The distributions of nearest-neighbor core separations are plotted in Fig. 11 for all starless cores (green histogram) and both *candidate* and *robust* prestellar cores (light and dark blue histograms, respectively). When deriving these distributions, each set of dense cores was analyzed separately, and only separations between cores of the same category were considered. The median nearest-neighbor core separation is similar, ~ 0.14 pc for all three samples. Interestingly, the histograms show steep rises (at ~ 0.07 pc) and falls (at ~ 0.2 pc), which bracket the characteristic ~ 0.1 pc inner width of nearby filaments (Arzoumanian et al. 2019).

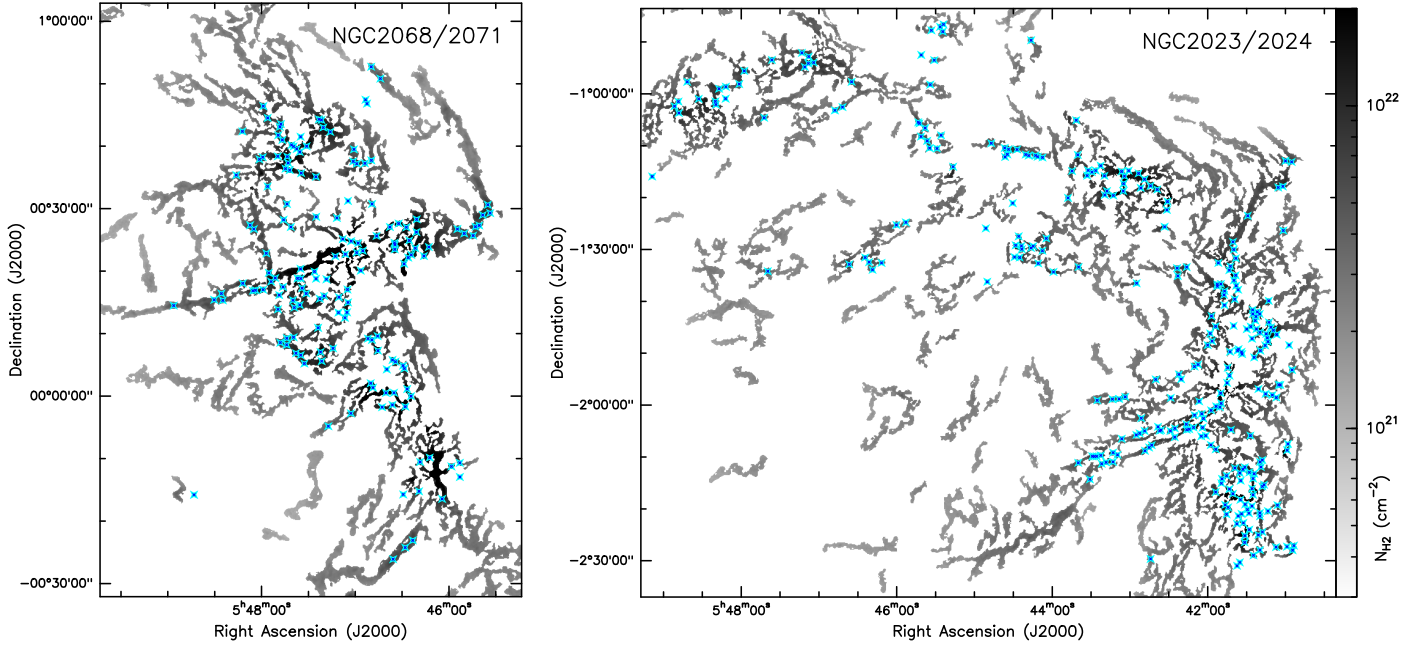


Fig. 9. Spatial distributions of *robust* prestellar cores (blue symbols) overplotted on the filament networks (gray background images) traced with *getfilaments* in NGC 2068 and 2071 (*left*), and NGC 2023 and 2024 (*right*). Transverse angular scales up to $100''$ across the filament footprints are shown here, corresponding to ~ 0.2 pc at $d = 400$ pc. In both panels, the color scale displayed within the filament mask corresponds to column density values in the original column density map (Fig. 2 left). See Fig. E.2 (right) for a similar view in the case of L1622.

Table 2. Fractions of cores associated with filaments in Orion B.

	<i>robust</i> prestellar	<i>candidate</i> prestellar	starless
<i>getfilaments</i> scales up to ~ 0.1 pc	87%	83%	72%
<i>getfilaments</i> scales up to ~ 0.2 pc	90%	87%	76%
<i>robust</i> DisPerSE filaments, 0.05 pc	60%	55%	43%
<i>robust</i> DisPerSE filaments, 0.1 pc	65%	60%	47%
<i>robust</i> DisPerSE filaments, 0.2 pc	71%	66%	53%
raw DisPerSE filaments, 0.05 pc	93%	89%	79%
raw DisPerSE filaments, 0.1 pc	97%	94%	85%
raw DisPerSE filaments, 0.2 pc	99%	97%	90%

Notes. This table gives fractions of prestellar and starless cores found within various *getfilaments* and DisPerSE mask images. For the *getfilaments* masks, upper transverse scales of either ~ 0.1 pc or ~ 0.2 pc (i.e., $\sim 50''$ or $\sim 100''$, respectively), were considered. The DisPerSE filament footprints were assumed to be 0.05, 0.1, or 0.2 pc-wide around the nominal filament crests, and both the *robust* and the raw sample of DisPerSE filaments (see Sect. 3.2 for details) were considered.

Similar distributions of nearest-neighbor core separations are found for the samples of Aquila cores from Könyves et al. (2015), for which the median nearest-neighbor core separation is 0.09 pc, and the most significantly rising and falling histogram bins are at separations of ~ 0.06 and ~ 0.1 pc, respectively.

4.2. Mass segregation of prestellar cores

Investigating how dense cores of different masses are spatially distributed (and possibly segregated) is of vital interest for understanding the formation and early dynamical evolution of embedded protostellar clusters.

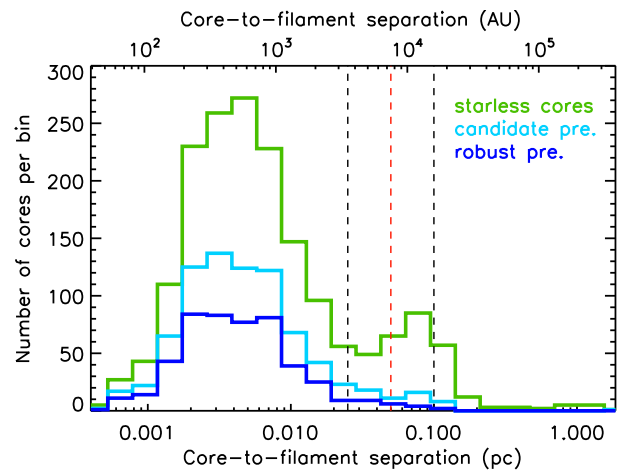


Fig. 10. Distribution of separations between dense cores and the nearest filament crests in the DisPerSE raw sample of filaments. The green histogram is for all 1768 starless cores, the light blue histogram for the 804 *candidate* prestellar cores, and the dark blue histogram for the 490 *robust* prestellar cores. The vertical lines mark the half widths (i.e., on either side of the filament crests) of a 0.1 pc-wide (red), 0.5×0.1 pc-wide (inner black), and a 2×0.1 pc-wide (outer black) filament.

Figure 12 shows the median mass of *candidate* prestellar cores as a function of ambient column density in the parent cloud. The upper panel displays the median core mass as observed in each column density bin before any correction for incompleteness effects, while the lower panel displays median core masses corrected for incompleteness. The incompleteness correction was achieved as follows, using the model completeness curves presented in Appendix C as a function of background column density (see Fig. C.4). In each bin of background column densities as estimated by *getsources*, each observed core mass

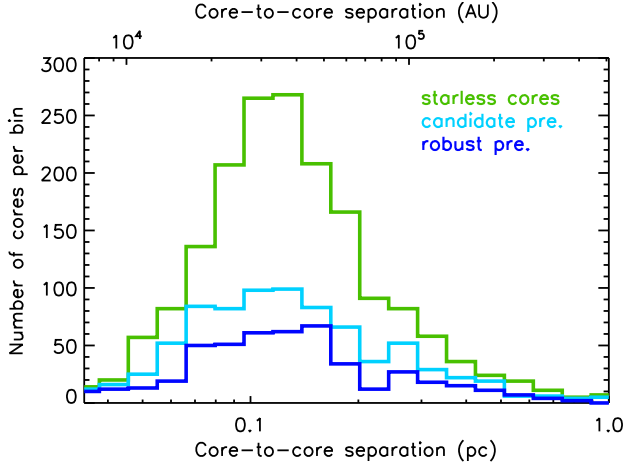


Fig. 11. Distribution of nearest-neighbor core separations in Orion B. The green, light-, and dark blue histograms show the distributions of nearest-neighbor separations for starless cores (either bound or unbound), *candidate* prestellar cores, and *robust* prestellar cores, respectively. In each case, only the separations between cores of the same category were considered. The median core separation is ~ 0.14 pc for all three core samples.

was weighted by the inverse of the model completeness fraction before computing the weighted median mass and interquartile range for that bin. It can be seen in Fig. 12 that both the median prestellar core mass and the dispersion in core masses increase with background column density. Moreover, this increase in core mass and mass spread is robust and not dominated by incompleteness effects which make low-mass cores somewhat more difficult to detect at higher background column densities (see lower panel of Fig. 12).

Taking differential incompleteness effects into account (cf. Fig. C.4), this suggests that both higher- and lower-mass prestellar cores may form in higher density clumps and filaments, a trend also seen in the Aquila cloud (cf. André et al. 2017). A simple interpretation of this trend is that the effective Jeans mass increases roughly linearly with background column density, because the velocity dispersion is observed to scale roughly as the square root of the column density (see, e.g., Heyer et al. 2009; Arzoumanian et al. 2013), while the thermal Jeans mass decreases roughly linearly with background column density (see Eq. (1) of André et al. 2019).

4.3. Prestellar core mass function

The core mass functions derived for the samples of 1768 starless cores, 804 *candidate* prestellar cores, and 490 *robust* prestellar cores identified in the whole Orion B cloud are shown as differential mass distributions in Fig. 13 (green, light blue, and dark blue histograms, respectively). We note that all three distributions merge at high masses, which simply reflects the fact that all of the starless cores identified above $\sim 1 M_{\odot}$ are dense and massive enough to be self-gravitating, hence prestellar in nature.

The high-mass end of the prestellar CMF above $2 M_{\odot}$ is well fit by a power-law mass function, $\Delta N/\Delta \log M \propto M^{-1.27 \pm 0.24}$ (see Fig. 13), which is consistent with the Salpeter power-law IMF ($\Delta N/\Delta \log M_{\star} \propto M_{\star}^{-1.35}$ in the same format – Salpeter 1955). The black solid line in Fig. 13 is a least-squares fit. A non-parametric Kolmogorov-Smirnov (K-S) test (see, e.g. Press et al. 1992) confirms that the CMF above $2 M_{\odot}$ is consistent with a power-law

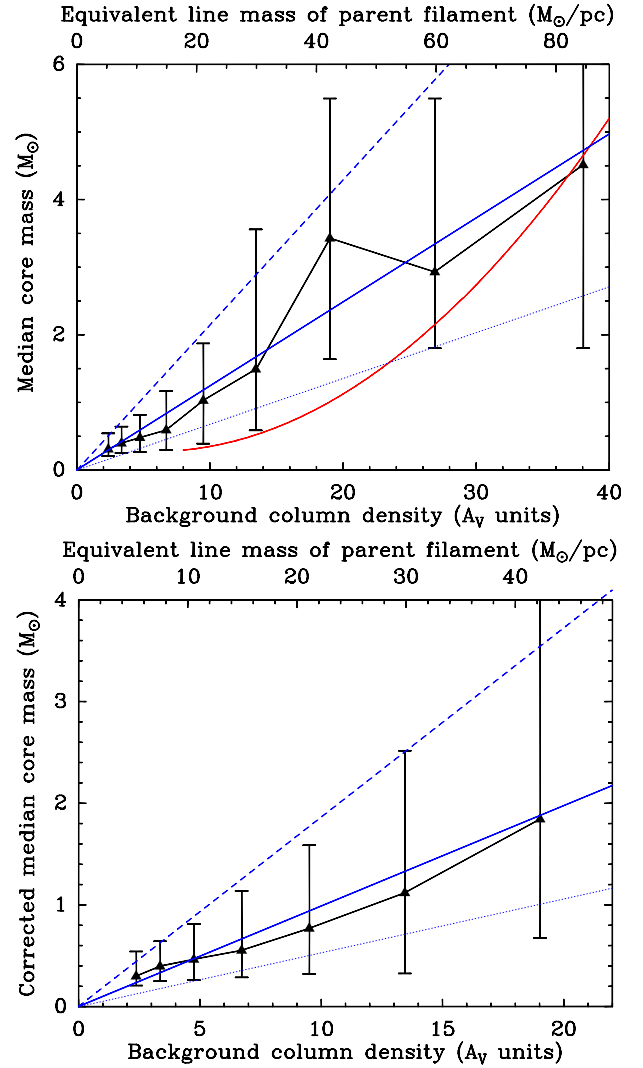


Fig. 12. *Top:* median prestellar core mass versus background column density (black triangles). The error bars correspond to the inter-quartile range in observed masses for each bin of background column density. The solid, dashed and dotted blue lines are linear fits to the observed median, upper-quartile, and lower-quartile masses as function of background column density, respectively. The red curve shows how the mass at the 50% completeness level varies with background column density according to the model completeness curves of Appendix C (see Fig. C.4). The upper x -axis provides an approximate mass-per-unit-length scale, assuming the local background around each core is dominated by the contribution of a parent filament with a characteristic width $W_{\text{fil}} = 0.1$ pc (see end of Sect. 4.5). *Bottom:* same as upper panel after correcting the distribution of observed core masses for incompleteness effects before estimating the median core mass and inter-quartile range in each column density bin (see Sect. 4.2). Both the median prestellar core mass and the dispersion in core masses increase roughly linearly with background column density.

mass function, $\Delta N/\Delta \log M \propto M^{-1.33 \pm 0.13}$, at a significance level of 95%.

The observed peak of the prestellar CMF at ~ 0.4 – $0.5 M_{\odot}$ is similar to that seen in the Aquila region (cf. Fig. 16 of Könyves et al. 2015) but is here extremely close to the estimated 80% completeness limit of $0.4 M_{\odot}$ in observed core mass (cf. Sect. 3.8 and Appendix C). It may therefore not be significant.

In order to further test the mass segregation result discussed in Sect. 4.2 above, Fig. 14 compares the CMF of *candidate*

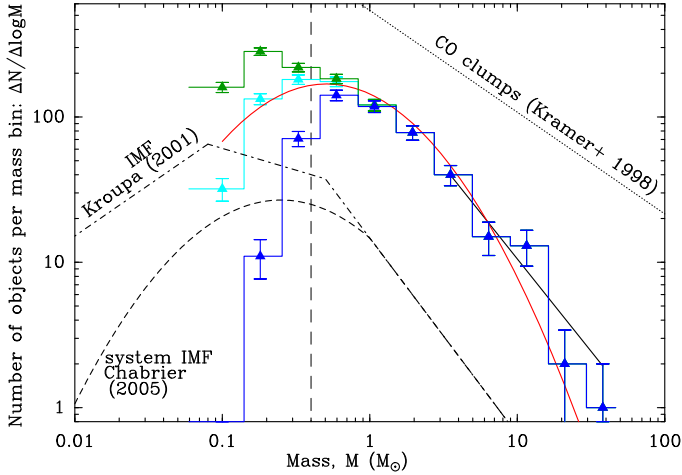


Fig. 13. Differential core mass function ($\Delta N/\Delta \log M$) of the 1768 starless cores (green histogram), 804 *candidate* prestellar cores (light blue histogram), and 490 *robust* prestellar cores (dark blue histogram) identified with *Herschel* in the whole Orion B field. The error bars correspond to \sqrt{N} statistical uncertainties, and the vertical dashed line shows the completeness limit of the prestellar sample at $\sim 0.4 M_{\odot}$. A lognormal fit to the CMF of *candidate* prestellar cores (solid red curve), as well as a power-law fit to the high-mass end of the CMF (black solid line) are superimposed. The lognormal fit peaks at $0.5 M_{\odot}$, and has a standard deviation of ~ 0.52 in $\log_{10} M$. The power-law fit has a slope of -1.27 ± 0.24 (compared to a Salpeter slope of -1.35 in this format). The IMF of single stars (corrected for binaries – e.g., Kroupa 2001), the IMF of multiple systems (e.g., Chabrier 2005), and the typical mass distribution of CO clumps (e.g., Kramer et al. 1998) are also shown for comparison.

prestellar cores observed at low and intermediate background column densities ($A_V^{\text{bg}} < 7$, purple histogram) with that observed at high background column densities ($A_V^{\text{bg}} \geq 15$, magenta histogram). It can be seen that the prestellar CMF observed at high background A_V values peaks at an order of magnitude higher mass than the prestellar CMF observed at low and intermediate background A_V values, that is, $\sim 3.8 M_{\odot}$ versus $\sim 0.4 M_{\odot}$, respectively. Indeed, the majority of prestellar cores found at low and intermediate A_V^{bg} have significantly lower masses than the majority of prestellar cores found at high A_V^{bg} , which corresponds to the findings of Sect. 4.2 (see Fig. 12). The split in background visual extinction at $A_V^{\text{bg}} < 7$ and $A_V^{\text{bg}} \geq 15$ was somewhat arbitrary, but similar –albeit less significant– results are obtained with other low and high background extinction limits.

Interestingly, a similar difference between the prestellar CMFs observed at high and low background A_V values is also seen in the Aquila cloud (André et al. 2017), and a related result was also found in Orion A, where Polychroni et al. (2013) reported two distinct mass distributions for cores “on” and “off” prominent filaments, that is, at high and low background A_V , respectively. We also note that, based on recent ALMA observations, Shimajiri et al. (2019) found a CMF peaking at $\sim 10 M_{\odot}$ in the very dense, highly supercritical filament of NGC 6334 (with $M_{\text{line}} \approx 500\text{--}1000 M_{\odot}/\text{pc} \gg M_{\text{line,crit}}$, corresponding to $A_V^{\text{bg}} \geq 100$), which is again consistent with the same trend.

4.4. Mass budget in the cloud

Using our *Herschel* census of prestellar cores and filaments, we can derive a detailed mass budget for the Orion B cloud. In the

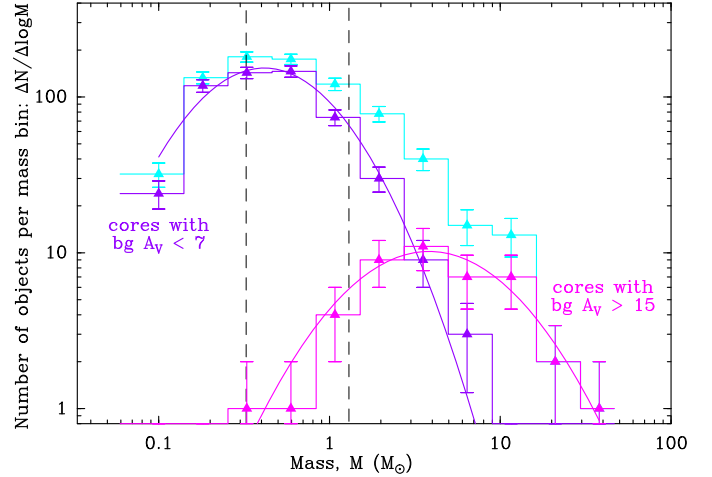


Fig. 14. Comparison of the differential CMF ($\Delta N/\Delta \log M$) derived for the 558 *candidate* prestellar cores lying in areas of low background column density ($A_V^{\text{bg}} < 7$, purple histogram) with the CMF of the 43 *candidate* prestellar cores lying in areas of high column density ($A_V^{\text{bg}} \geq 15$, magenta histogram). Lognormal fits are shown in both cases, and have peaks at $0.4 M_{\odot}$ and $3.8 M_{\odot}$, respectively. Vertical dashed lines show the 80% completeness limits of the low and high column density samples at $0.33 M_{\odot}$ and $1.3 M_{\odot}$, respectively. The overplotted histogram in light blue is the CMF of all 804 *candidate* prestellar cores (same as in Fig. 13).

intermediate column density regions ($A_V^{\text{bg}} \sim 3 - 7$), a large fraction, $\sim 60\%$, of the gas mass is in the form of filaments but only $\sim 3 - 5\%$ of the cloud mass is in the form of prestellar cores. In higher column density regions ($A_V^{\text{bg}} \geq 7$), a similarly high fraction of the cloud mass is in the form of filaments and a fraction $f_{\text{pre}} \sim 22\%$ of the mass is in the form of prestellar cores.

In an attempt to quantify further the relative contributions of cores and filaments to the cloud material as a function of column density, we compare in Fig. 15 the column density PDFs observed for the cloud before any component subtraction (blue histogram, identical to the PDF shown in Fig. 4 left), after subtraction of dense cores (red solid line), and after subtraction of both dense cores and filaments (black solid line). To generate this plot, we used *getsources* to create a column density map of the cloud after subtracting the contribution of all compact cores, and *getfilaments* to construct another column density map after also subtracting the contribution of filaments. Although there are admittedly rather large uncertainties involved in this two-step subtraction process, the result clearly suggests that filaments dominate the mass budget in Orion B throughout the whole column density range. In the Lupus region, Benedettini et al. (2015) also found that the power-law tail of their PDF is dominated by filaments.

4.5. Column density transition toward prestellar core formation

The existence of thresholds for star formation have been suspected for a long time, based on the results of ground-based millimeter and submillimeter surveys for cores in, for instance, the Taurus, Ophiuchus, and Perseus clouds (e.g., Onishi et al. 1998; Johnstone et al. 2004; Hatchell et al. 2005). Following these early claims, the HGBS results in Aquila and Taurus provided a much stronger case for a column density threshold for prestellar core formation (André et al. 2010; Könyves et al. 2015;

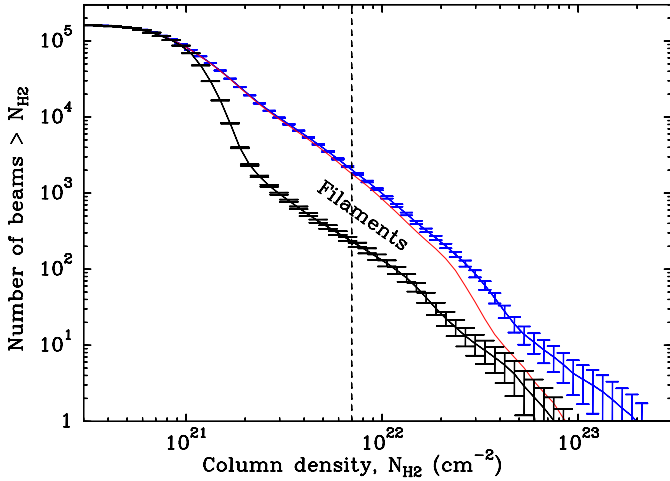


Fig. 15. Comparison of the global column density PDF in Orion B (blue histogram) to the column density PDF measured after subtraction of dense cores (red solid line) and the PDF measured after subtraction of both dense cores and filaments (black solid line with statistical error bars). The blue histogram is identical to that shown in Fig. 4 (left). The vertical dashed line marks the approximate separation between low-to-intermediate and high column density values at $A_V^{\text{bg}} \sim 7$.

Marsh et al. 2016) thanks to the excellent column density sensitivity and high spatial dynamic range of the *Herschel* imaging data, making it possible to probe prestellar cores and the parent background cloud simultaneously. The *Herschel* results on the characteristic inner width of filaments (Arzoumanian et al. 2011, 2019) and the tight connection observed between cores and filaments (cf. Sect. 4.1.1) also led to a simple interpretation of this threshold in terms of the critical mass per unit length of nearly isothermal cylinder-like filaments (André et al. 2014).

To investigate whether a column density threshold for core formation is present in Orion B, and following the study of Könyves et al. (2015) in Aquila, we plot in Fig. 16 the differential prestellar core formation efficiency $\text{CFE}_{\text{obs}}(A_V) = \Delta M_{\text{cores}}(A_V) / \Delta M_{\text{cloud}}(A_V)$ as a function of the background cloud column density in the Orion B complex. This was obtained by dividing the mass $\Delta M_{\text{cores}}(A_V)$ of the *candidate* prestellar cores identified with *Herschel* in a given bin of background column densities (expressed in A_V units) by the total cloud mass $\Delta M_{\text{cloud}}(A_V)$ in the same bin. It can be seen in Fig. 16 that $\text{CFE}_{\text{obs}}(A_V)$ exhibits a step rise in the vicinity of $A_V^{\text{bg}} \sim 7$ and resembles a smooth step function, fairly similar to that observed in the Aquila cloud (see Fig. 12 of Könyves et al. 2015). The *Herschel* observations indicate a sharp transition between a regime of very low CFE_{obs} at $A_V^{\text{bg}} < 5$ and a regime where $\text{CFE}_{\text{obs}}(A_V)$ is an order of magnitude higher and fluctuates around a roughly constant value of $\sim 15\text{--}20\%$. The combination of this sharp transition with the column density PDF of Fig. 4 implies that, at least in terms of core mass, most prestellar core formation occurs just above $A_V^{\text{bg}} \sim 7$ (see top panel of Fig. 17). Based on Figs. 16 and 17 (top panel), we argue for the presence of a true physical “threshold” for the formation of prestellar cores in Orion B around a fiducial value $A_V^{\text{bg}} \sim 7$, which we interpret here as well as resulting from the mass-per-unit-length threshold above which molecular filaments become gravitationally unstable. It should be stressed, however, $A_V^{\text{bg}} \sim 7$ is only a *fiducial* value for this threshold, which for various reasons should rather be viewed as a smooth transition (see discussion in André et al.

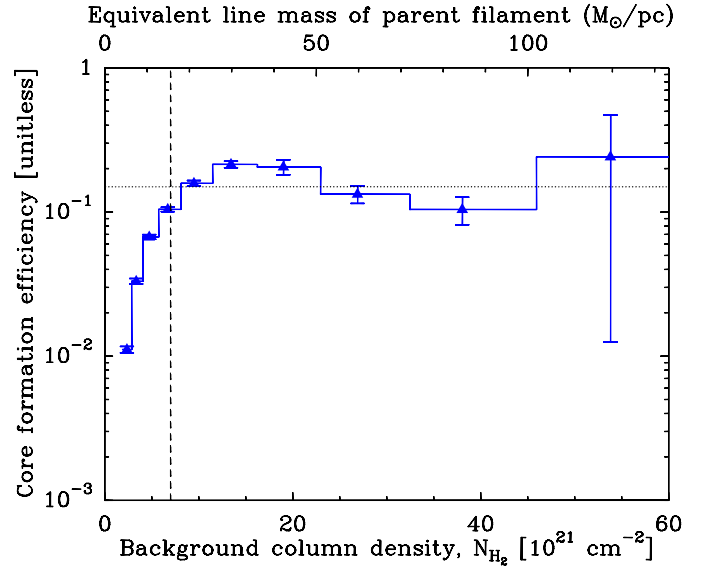


Fig. 16. Differential core formation efficiency (CFE) as function of ambient cloud column density expressed in A_V units (blue histogram with error bars), obtained by dividing the mass in the form of *candidate* prestellar cores in a given column density bin by the cloud mass observed in the same column density bin. The upper x -axis provides an approximate mass-per-unit-length scale, assuming the local background around each core is dominated by the contribution of a parent filament with a characteristic width $W_{\text{fil}} = 0.1$ pc (see end of Sect. 4.5). The vertical dashed line marks the fiducial threshold at $A_V^{\text{bg}} \sim 7$. The horizontal dotted line marks the rough asymptotic value of $\sim 15\%$ for the CFE at $A_V > 15$.

2014). We also note some environmental variations in the details of this transition between Orion B and Aquila. In Orion B, the raw number of prestellar cores per column density bin peaks at $A_V^{\text{bg}} \sim 3$ (see bottom panel of Fig. 17) or at most at $A_V^{\text{bg}} \sim 5\text{--}6$ if we take into account a correction factor $A_{V,\text{HGBS}}/A_{V,\text{ext}} \sim 0.5\text{--}0.6$ between the A_V^{bg} values derived from the HGBS column density map and those derived from near-infrared extinction maps in the range $A_V = 3\text{--}7$ mag (see Sect. 3.1). In Aquila, the raw number of prestellar cores peaks at a significantly higher background column density $A_V^{\text{bg}} \sim 8$ (see Fig. 11a of Könyves et al. 2015). Despite this difference, the shapes of the prestellar core formation efficiency as a function of background A_V , $\text{CFE}_{\text{obs}}(A_V)$, are remarkably similar in the two clouds (compare Fig. 16 here with Fig. 12 of Könyves et al. 2015).

Core formation efficiency is discussed as a function of background column density or A_V^{bg} here, as column density is the most directly observable quantity, but we can also provide a rough conversion in terms of background volume density and mass per unit length. In the 0.1-pc filament paradigm of core formation (André et al. 2014), the local background is dominated by the parent filament of each core and there is a direct correspondence between the average values of the surface density $\Sigma_{\text{fil}} \equiv \mu_{\text{H}_2} m_{\text{H}} N_{\text{H}_2}^{\text{fil}}$, volume density $\rho_{\text{fil}} \equiv \mu_{\text{H}_2} m_{\text{H}} n_{\text{H}_2}^{\text{fil}}$, and line mass M_{line} of the parent filament. For a cylindrical parent filament of width W_{fil} , one has: $\langle \Sigma_{\text{fil}} \rangle = M_{\text{line}} / W_{\text{fil}}$ and $\langle \rho_{\text{fil}} \rangle = 4 M_{\text{line}} / (\pi W_{\text{fil}}^2) = 4 \langle \Sigma_{\text{fil}} \rangle / (\pi W_{\text{fil}})$. In particular, adopting a uniform filament width $W_{\text{fil}} = 0.1$ pc, the fiducial column density threshold at $A_V^{\text{bg}} \sim 7$ corresponds to a threshold line mass $M_{\text{line,th}} \sim 15 M_{\odot} \text{pc}^{-1}$, very close to the thermal value of the critical mass per unit length $M_{\text{line,crit}} \sim 16 M_{\odot} / \text{pc}$ for $T \sim 10$ K